Particle morphology and electrostatic screening shape salinity-dependent flocculation and settling of fine blasted tunnel sediments

Franco Tapia[1], Franziska Lorz[1], Gerit Hartmut Orzechowski[1], Øyvind A. Thiem[2], Andrew Gravelle[2], Bernhard Vowinckel[1]

[1] Institute of Urban and Industrial Water Management, Technische Universität Dresden, Dresden, Germany
[2] Statens vegvesen (Norwegian Public Roads Administration), Bergen, Norway

Email addresses

Franco Tapia	franco.tapia@tu-dresden.de
Franziska Lorz	franziska.lorz@tu-dresden.de
Gerit Hartmut Orzechowski	gerit.orzechowski@tu-dresden.de
Øyvind A. Thiem	oyvind.thiem@vegvesen.no
Andrew Gravelle	andrew.gravelle@vegvesen.no
Bernhard Vowinckel	Bernhard.vowinckel@tu-dresden.de

Preprint statement

This manuscript is a non-peer-reviewed preprint submitted to EarthArXiv. The manuscript is intended for submission to Water Research.

Particle morphology and electrostatic screening shape salinity-dependent flocculation and settling of fine blasted tunnel sediments

Franco Tapia[a], Franziska Lorz[a], Gerit Hartmut Orzechowski[a], Øyvind A. Thiem[b], Andrew Gravelle[b], Bernhard Vowinckel[a]

[a]*Institute of Urban and Industrial Water Management, Technische Universität Dresden, Dresden, 01062, Germany*
[b]*Statens vegvesen, (The Norwegian Public Roads Administration), Bergen, Norway*

Abstract

Rock-blasted fine-grained sediments generated during tunnel excavation may enter receiving waters that range from freshwater to marine conditions. Yet the combined roles of primary-particle morphology and salinity-dependent electrostatic interactions in their settling remain poorly understood. In this work, fine sediments from five Norwegian tunnel construction sites were investigated using bulk-settling experiments over 0–35 PSU, microscopy-based particle characterization, and ζ-potential measurements. Bulk particle settling exhibited two distinct regimes. At low salinity, settling was weakly dependent on salt concentration but differed substantially between sites. These differences correlated with a morphology–size index $\mathcal{M}$ combining particle size and aspect ratio, indicating that primary-particle geometry conditions the baseline clarification response. At intermediate salt concentration, the suspensions underwent a marked transition toward enhanced settling, with operational critical coagulation concentrations between approximately 0.36 and 1.60 PSU. The magnitude of this salinity-induced clarification correlated with the change in ζ-potential, linking the macroscopic settling transition to the electrokinetic response of the suspended fraction. At higher salinity, clarification approached a common high-clarification regime. The results indicate that morphology and electrostatic interactions govern complementary stages of the settling process: primary-particle geometry conditions the low-salinity clarification state, whereas increasing salt concentration activates additional flocculation and clarification of the remaining sediments in suspension. This coupled framework provides a basis for predicting the fate of tunnel-derived fine sediments discharged into freshwater, brackish, and marine receiving environments.

Keywords:
Fine sediment settling, Flocculation, Salinity, Particle morphology, Zeta potential

1. Introduction

Fine mineral sediments originating from geological and anthropogenic sources can exhibit markedly different transport and settling behavior in aquatic environments. Coagulation and flocculation regulate the formation and growth of cohesive aggregates and consequently influence their settling velocity, persistence in suspension, transport, and potential ecological effects [1]. These processes depend on particle mineralogy and surface chemistry, together with the ionic composition of the receiving water, and can strongly affect water-column turbidity and clarification [2, 3]. Because colloidal particles possess a large specific surface area and abundant reactive surface sites, they may also facilitate or impede the transport of particle-associated contaminants between the water column and the sediment bed [4, 5]. Following deposition, excessive fine sediment can modify habitat conditions and impair the structure and functioning of benthic communities in both marine and freshwater environments [6, 7].

This problem is particularly relevant for anthropogenic sediments generated by blasting, crushing, drilling, and excavation. In contrast to naturally weathered material, freshly produced tunnel sediments commonly contain angular, sharp, or splintered mineral fragments and may be associated with site-specific contaminants and construction residues [8]. Their physicochemical behavior therefore depends not only on the geological composition of the excavated rock, but also on construction practices and the chemistry of the receiving water. Depending on the location and hydrological setting of the excavation sites, these particles may enter freshwater systems or brackish and marine receiving waters, where changes in salinity can substantially modify their aggregation, settling, and dispersal [2, 9].

In dilute suspensions, the rate of aggregation is commonly described through the combined effects of a transport-controlled collision frequency and an interaction-controlled collision efficiency. Collision frequency quantifies the rate of potential particle encounters generated by mechanisms such as Brownian diffusion, fluid shear, turbulence, and differential settling [10, 11]. Collision efficiency describes the fraction of these potential encounters that reach contact after hydrodynamic interactions and interparticle forces are taken into account [12]. Once contact occurs, the formation of a persistent aggregate additionally depends on the probability of attachment, although collision and attachment efficiencies are frequently combined into a single effective aggregation efficiency [13, 14].

Mineral surfaces immersed in water generally acquire an

electrical charge and become surrounded by an electrical double layer formed by dissolved ions from the surrounding electrolyte. At low salt concentration, the diffuse part of this layer extends farther into the liquid, producing a longer-ranged repulsive interaction between similarly charged particles and thereby stabilizing the suspension. Increasing salt concentration reduces the characteristic double-layer thickness and screens electrostatic repulsion, allowing attractive interactions, particularly van der Waals forces, to promote particle contact and aggregation [3, 12, 14]. Mineral assemblage, reactive fine phases, and surface coatings can modify surface charging and the corresponding ζ-potential response, although bulk mineralogy alone may not fully predict the electrokinetic behavior of complex natural sediments [3, 4].

The onset of rapid coagulation is commonly characterized by the critical coagulation concentration (CCC), defined for a given particle-electrolyte system as the electrolyte concentration above which the repulsive energy barrier is sufficiently reduced for aggregation to proceed in the rapid regime [1, 14]. Natural and engineered clay suspensions may consequently exhibit weakly salinity-dependent settling at low salt concentration, followed by enhanced flocculation and clarification over an intermediate salinity range [2, 15]. In bulk-settling experiments, this destabilization can appear as a transition from a low-salinity clarification plateau toward more rapid settling as salinity increases.

Although electrostatic interactions provide a central mechanism for salinity-induced coagulation, electrokinetic information alone is insufficient to predict the resulting bulk-settling response. The ζ-potential provides an operational descriptor of the electrostatic state of a suspension, but the relation between electrokinetic properties and flocculation remains conditioned by additional processes controlling particle encounters, attachment, and aggregate growth [12, 16]. Experiments comparing particles with similar characteristic size and electrokinetic conditions have further shown that differences in particle shape can produce substantially different sedimentation rates [17]. Consequently, sediments with comparable electrokinetic states may still exhibit different clarification dynamics, as settling additionally depends on particle size, morphology, density, porosity, and the structure of the resulting aggregates [18, 19].

Primary-particle morphology represents an additional source of variability that remains comparatively poorly constrained in salinity-dependent settling. Irregular and elongated particles differ from spherical particles not only in their hydrodynamic response, but also in the geometry and persistence of particle–particle contacts. Numerical studies of complex-shaped colloids show that geometric interlocking and entanglement can promote persistent particle associations even without attractive surface interactions [20]. In natural sediments, settling potential cannot be described by particle size alone, with shape, density, and porosity also contributing to particle dynamics [18]. Once aggregates form, their three-dimensional geometry and internal structure introduce additional controls on drag and settling, making simplified geometric representations increasingly inaccurate for complex flocs [19, 21]. Primary-particle morphology may therefore influence the initial aggregation pathway, while the structure of the resulting flocs further conditions their subsequent settling behavior.

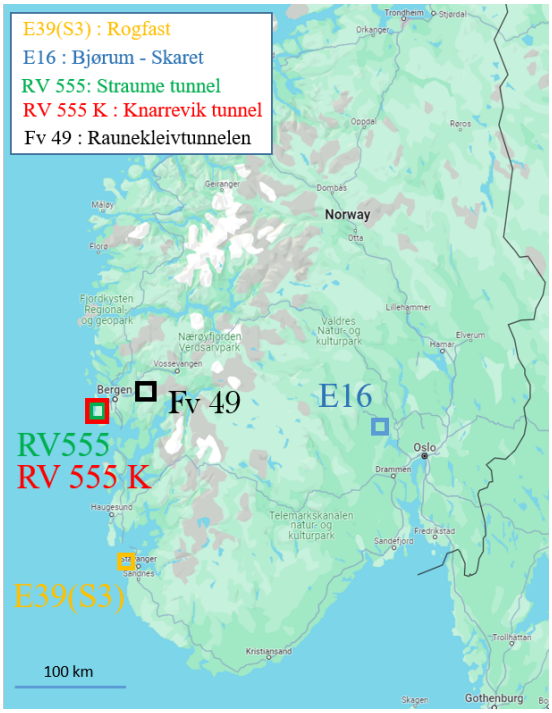

Figure 1: Geographic location of the sampling sites in western Norway. Sediments were collected from five tunnel construction projects: E39(S3) (Rogfast, yellow), E16 (Bjørum - Skaret, blue), RV555 (Straume tunnel, green), RV 555 K (Knarrevik tunnel, red), and Fv49 (Raunekleivtunnelen, black).

This coupling is particularly relevant for tunnel-derived sediments, which contain freshly generated, angular and splintered rock fragments whose properties vary with geology and excavation history. Previous studies of Norwegian tunneling waters have primarily addressed suspended-solids loads, treatment requirements, and the efficiency of sedimentation or chemical coagulation [8], while recent investigations of blasted-rock disposal in fjords have focused on the bulk dynamics and dispersal of polydisperse rock releases [9]. Comparatively little attention has been given to how the primary-particle morphology of the fine fraction interacts with salinity-dependent electrostatic destabilization to determine clarification across sediments from different tunnel sites. The present study addresses this gap by combining bulk-settling experiments over freshwater-to-marine salinities with microscopy-derived particle morphology and ζ-potential measurements for fine blasted and crushed sediments collected from five Norwegian tunnel projects.

2. Materials and Methods

2.1. Sediments and mineralogical characterization

Sediment samples were collected from five tunnel excavation sites in western Norway representing various geological settings and processing histories (Fig. 1). The E39(S3) sample was obtained from the Rogfast tunnel (Kvitsøy), where the process water generated in the excavation process is treated in

Mineral	E39(S3)	E16	RV 555	RV 555K
Quartz	7.0	7.2	26.8	17.1
K-feldspar (microcline)	–	26.7	27.1	14.6
Plagioclase (albite-rich)	11.8	33.9	14.0	26.7
Amphibole group	25.7	–	–	–
Clinopyroxene	4.0	–	–	–
Epidote	6.8	1.7	5.8	13.7
Titanite	4.2	–	–	–
Calcite	4.9	2.1	3.9	4.4
Hematite	–	7.0	0.8	1.3
Biotite	3.1	–	–	–
Muscovite-illite	–	12.5	17.3	3.1
Chlorite group	23.8	3.2	4.3	12.9
Smectite group, dioctahedral	8.7	–	–	6.2
Dolomite-ankerite	–	–	–	5.4
Apatite	–	0.3	–	–

Table 1: Mineralogical composition of the investigated sediment samples determined by XRD (Rietveld refinement; Co-Kα, Orion Comet P2; BGMN/Profex). All values are relative mass-% of the crystalline fraction, with crystalline phases normalized to 100 wt.%. "–" = not detected / below detection limit.

a multi-stage cleaning facility. Sediments at this site are labeled according to their treatment stage, and the present study focuses on the fine fraction collected at the final stage of an indoor settling tank, denoted E39(S3). The E16 sample was collected from the Bjørum–Skaret site, where material was obtained directly from excavation sites without prior water treatment. The RV 555 sample was collected from freshly blasted material in the Straume tunnel (west corridor, approximately 150 m from the eastern entrance of the tunnel), providing a dataset dominated by fresh, minimally weathered mineral fragments. The RV 555 K sample was collected from the Knarrevik tunnel (Sotra connection), representing material influenced by a different fjord-side geological setting. The Fv 49 sample was collected from the Raunekleivtunnelen, where the tunnel intersects serpentinite-rich formations containing chrysotile asbestos. This material is particularly interesting because of its fibrous morphology and environmental relevance.

The mineralogical composition of the sediments was determined by X-ray powder diffraction (XRD) with Rietveld refinement at the Institute of Mineralogy, TU Bergakademie Freiberg. Measurements, summarized in Table 1, were conducted using an Orion Comet P2 diffractometer with Co-Kα radiation, and phase quantification was performed with the BGMN/Profex software package. The identified crystalline phases were normalized to 100 wt% of the crystalline fraction.

As summarized in Table 1, the analyzed sediments span contrasting mineralogical assemblages, ranging from quartz–feldspar-rich compositions to samples with a stronger contribution from chlorite-, amphibole-, and smectite-related phases. The sample Fv 49 is not included in Table 1 because it was treated separately in this study as a reference material rich in chrysotile-asbestos.

2.2. Bulk Settling Experiment

To quantify the settling response of the investigated sediments under controlled chemical conditions, bulk-settling experiments were carried out across a salinity range representative of conditions ranging from fresh water to seawater. The aim was to compare the clarification kinetics between sites and to determine how changes in salinity modify the transition from weak aggregation and slow settling to enhanced flocculation and more rapid settling.

The settling tests were performed using a protocol adapted from [15]. Suspensions were prepared in cell-culture flasks (Carl Roth, article number CE48.1) with characteristic internal dimensions of $7.5 \times 3.6 \times 1.7$ cm^3. These dimensions describe the geometry of the flask used for the settling measurements and should not be interpreted as the total volumetric capacity of the vessel. Each flask was filled with approximately 69 mL of suspension, corresponding to a vertical settling distance of 7.5 cm. Sediment and sodium chloride masses were measured using a precision balance (Sartorius Handy, Type H160-V20; resolution 0.001 g). Sodium chloride was supplied by Fisher Scientific (code S/3120/65, laboratory reagent grade, purity $\geq 99.5\%$).

Before suspension preparation, the sediments were dried at 60°C for 1 h and sieved through a 200 μm mesh to exclude coarse grains and restrict the analysis to the fine sediment fraction relevant to suspension and flocculation processes. The sediment concentration in water was fixed at 8 ppt, where parts per thousand (ppt) is used here as a mass concentration equivalent to 8 g L^{-1} of sediment. Salinity was varied from 0 to 35 PSU, where Practical Salinity Units (PSU) are used operationally in this study to denote the nominal NaCl concentration in g L^{-1}. Thus, 35 PSU corresponds to approximately 35 g L^{-1} of added NaCl, while 0 PSU corresponds to deionized (DI) water with an electrical conductivity of 4.7 μS cm^{-1}. The pH remained within a narrow circumneutral range of 7.3–8.0 throughout the experiments. Previous measurements on cohesive mud showed only weak variations in ζ-potential at pH values above approximately 4, whereas decreasing the pH toward acidic conditions substantially enhanced floc formation [16]. Given the limited pH variation observed here and the absence of acidic conditions, pH is therefore expected to have only a secondary influence on the measured settling response compared with the imposed changes in salinity. The pH and electrical conductivity of the suspensions were measured using a WTW Multi 3430 IDS multiparameter meter (Wissenschaftlich-Technische Werkstätten GmbH, Weilheim, Germany).

After preparation, each suspension was placed in an ultrasonic bath (VWR USC 300 TH ultrasonic cleaner, 2,8 Lts, 45 kHz) for 20 min at 22°C in order to disperse preexistent clusters. Immediately before each run, the suspensions were homogenized by orbital shaking for 60 s using a platform shaker (LABOSHAKE, typeRO 5, Gerhardt Bonn) operated at a frequency of 1.8 Hz and a stroke length of 5 cm. This configuration produced a maximum velocity of 28.75 cm s^{-1} and an acceleration of 3.3 m s^{-2}. The flasks were then placed in a rack with fixed marked positions to ensure consistent alignment (Fig. 2). This transfer required approximately 10 s before image acquisition started. The rack was illuminated with a backlight using a light panel (Walimex Pro Soft LED 200 Flat Bi Color, article number 21243) operated at 10% intensity and a color temperature of 4400 K. The panel was positioned at a distance

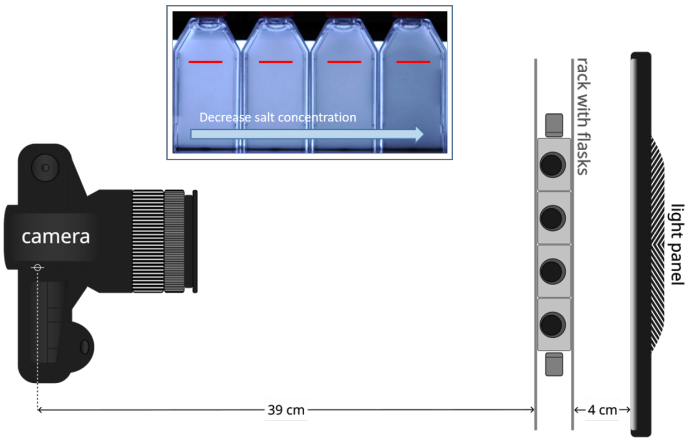

Figure 2: Schematic top-view representation of the experimental setup used to monitor bulk settling under controlled optical conditions. A camera records the flask rack in backlight configuration, allowing the temporal evolution of transmitted light intensity to be quantified at a fixed observation level. The inset shows a representative example of experimental data for E39(S3), highlighting the horizontal observation level (red lines) and the decrease in salt concentration from left to right across the flasks.

of 4.0 cm from the rack to provide homogeneous illumination while minimizing heat transfer. This configuration maintained a stable working temperature of approximately 22°C throughout the experiments. The settling process was continuously monitored with a single-lens digital reflex camera (Canon EOS 1000D), equipped with an EF-S 18-135 mm lens, using an aperture of f/7.1 and a shutter speed of 1/100 s. The images were acquired under backlight conditions from a distance of 39.0 cm every 5 min for up to 8 h. The recorded images were subsequently processed in Python 3.

The setup shown in Fig. 2 was used to quantify the temporal evolution of particle concentration in suspension. A fixed observation level was defined at 5 cm height and 1.5 cm width, within each flask, as illustrated by the red horizontal line in the inset of Fig. 2, and the corresponding grayscale values were tracked along this horizontal line. The grayscale value serves as a proxy for suspended particle concentration: darker values indicate higher particle concentrations. The average value recorded over the entire observation level is referred to here as the transmitted light intensity I. For the settling analysis, the transmitted light intensity was normalized using two reference states: the initial intensity at $t = 0$, denoted I_0, and the asymptotic intensity after complete or quasi-complete sedimentation, denoted I_∞, measured after 48 h. The use of I_∞ corrects for residual light attenuation that is not related to suspended particles, mainly due to (i) the optical transmission of the plastic flask walls and (ii) possible adhesion of sediment to the walls. In practice, wall adhesion was negligible under properly prepared conditions, and no significant differences in optical transmission were observed between flasks. The normalization was calculated individually for each flask and salinity condition. The normalized transmitted light intensity is defined as

$$I_{\mathrm{norm}}(t) = \frac{I(t) - I_0}{I_\infty - I_0}, \tag{1}$$

where $I(t)$ is the transmitted light intensity measured at time t.

A critical artifact was the presence of air bubbles, which could locally enhance particle attachment and bias I_∞ by creating persistent light-scattering or adhesion zones. Experiments in which bubbles were observed were therefore discarded and repeated to ensure reproducibility and consistency of the normalized intensity signal.

2.3. Microscopy Analysis

Direct observation provides immediate access to the shape and size of the particles. In order to visualize and quantify the aspect ratio and the average particle size, we used a high-resolution microscope (Leica MD 6000B) equipped with a 20× objective, connected to a digital camera (1392 × 1040 px^2), allowing a resolution of 2 $px/\mu m$. To ensure a homogeneous suspension, 0.01 g of sediments were dispersed in a mixture of 800 μL of DI-water based dispersant (DIN ISO 11277:2002-08; 16.5 g of sodium diphosphate, 3.5 g of sodium carbonate, and 500 mL of DI water) and 500 μL of glycerol. Subsequently, they were stirred vigorously for 10 s before sampling using a mixing device (IKA VORTEX 2). The samples were then extracted from various locations within the container using a 15 μl-pipette to minimize the selection biases in particle size caused by early sedimentation. Finally, the extracted samples are carefully placed between two microscope cover glasses for direct observation under the microscope. For each detected particle, their projected major and minor axes are denoted by d_1 and d_2, respectively. The particle size was defined as the arithmetic mean of these two characteristic lengths, $d = (d_1 + d_2)/2$, and the aspect ratio as $\alpha = d_1/d_2$. This definition provides a first-order geometrical description of particle morphology in a 2D-projection, in which d represents an effective size and α characterizes particle elongation.

2.4. ζ-potential measurements

The ζ-potential was measured on the same dried and sieved sediment stocks used in the bulk-settling experiments, without dispersant, using a Malvern Zetasizer Nano equipped with a DTS1070 cuvette. Salinity was varied from 0 to 35 PSU, with intermediate values selected to resolve from low-salinity to high-salinity regime (typically 0, 0.01, 0.03, 0.1, 0.7, 1.5, 2, 5, 10, and 35 PSU). Measurements were carried out at room temperature (~ 22 °C). For each salinity, the suspension was gently homogenized, transferred to the cuvette while avoiding air bubbles, and measured using the default ζ-potential protocol. Four replicate measurements were recorded per condition, and the resulting data were exported and post-processed in Python 3 for plotting and comparison with the bulk-settling response.

3. Results

3.1. Bulk settling response across sites

We first examine changes in bulk settling behavior of the investigated sediments under increasing salinity. The objective of this section is to compare how the bulk clarification dynamics vary across different sites and identify the salinity range over which the response changes most strongly.

The normalized transmitted light intensity, I_{norm}, is shown as a function of time in Fig. 3(a)–(e) for E39(S3), E16, RV 555, RV 555 K, and Fv 49, respectively. In all cases, I_{norm} increases monotonically with time, indicating progressive clarification, although both the settling rate and its sensitivity to salinity differ markedly between sites. A common feature is that, at relatively low salinity (warm colors in Fig. 3a–e) and at high salinity (blue colors), the settling response becomes weakly dependent, or nearly insensitive, to salt concentration, whereas at intermediate salt concentrations ($0.1 \lesssim s \lesssim 5$ PSU) the settling rate is strongly site-dependent. Furthermore, although the low-salinity regime exhibits little sensitivity to salinity, it still shows clear site-to-site differences in the settling kinetics, with RV 555 displaying the slowest clarification under these conditions (Fig. 3c).

To compare the dependence of bulk settling behavior on salinity more directly, the normalized transmitted light intensity was evaluated at a fixed observation time, $T = 4$ h. This time was selected as a common comparison window and corresponds, for all samples, to the timescale over which the highest-salinity suspension had essentially completed its settling. The values of I_{norm} are therefore plotted as a function of salt concentration in Fig. 3(f). The data shown in this figure exhibit a sigmoidal increase with salinity s, consistent with a transition from weakly salt-dependent slow settling at low salinity to enhanced flocculation and faster clarification at higher salinity.

We follow the procedure by [15] to quantify this transition. Toward this end, the data were fitted using the error-function form

$$I_{\mathrm{norm}}(s) = A\,\mathrm{erf}\left[B\,\log_{10}\left(\frac{s}{s_{\mathrm{CCC}}}\right)\right] + D \qquad , \tag{2}$$

where A, B, and D are fitting parameters and s_{CCC} denotes the salinity that marks the inflection point of the fit. The corresponding fitting curves for their respective data sets from the different sites are shown as dashed lines in Fig. 3(f). In the present work, s_{CCC} is used as an operational estimate of the critical coagulation concentration [22], i.e. a CCC-like salinity at which the settling response changes most rapidly. Because the fit is evaluated at a fixed observation time, these parameters are time-window dependent and should therefore be interpreted primarily as comparative descriptors rather than as absolute material constants. In this sense, they provide a consistent framework for comparing the relative effects of salinity and site-specific sediment properties on the bulk-settling response. [15] analyzed the sensitivity of s_{ccc} on the choice of T for bentonite samples and found only little dependency of ±15%. The fitting parameters obtained from Eq. 2 for all samples determined at $T = 4$ h are summarized in Table 2.

The fit parameters reveal clear inter-site differences in the salinity-dependent settling response. In particular, RV 555 exhibits the largest transition amplitude, corresponding to the largest increase in normalized transmitted light intensity between the low- and high-salinity regimes ($A = 0.27\pm0.01$). This indicates that RV 555 undergoes the strongest salinity-induced enhancement in clarification. By contrast, Fv 49 shows an almost negligible amplitude ($A \approx 0$), indicating only weak sensitivity to salinity over the investigated range. The characteristic inflection salinity also differs substantially between samples, ranging from $s_{\mathrm{CCC}} = 0.36\pm0.07$ PSU for E16 to 1.60 ± 0.05 PSU for RV 555, while E39(S3) and RV 555 K exhibit intermediate values. Geometrically, the parameters in Eq. 2 describe complementary features of the sigmoidal response: A represents half of the vertical distance between the low- and high-salinity plateaus, D gives the value of I_{norm} at the inflection point and therefore sets the vertical position of the curve, B controls the sharpness of the transition in logarithmic salinity space, and s_{CCC} sets its horizontal position. Accordingly, the asymptotic plateau values are given by $D - A$ at low salinity and $D + A$ at high salinity, while the maximum slope occurs at $s = s_{\mathrm{CCC}}$. The tendency of the high-salinity responses to converge above approximately 5 PSU is therefore reflected by similar values of $D + A$, whereas the pronounced site dependence of the low-salinity plateau is captured by differences in $D - A$. A more detailed interpretation of these parameters and their time dependence is provided in the Discussion.

Importantly, settling is enhanced over the full salinity range investigated, while the additional enhancement associated with increasing salt concentration becomes particularly pronounced over the intermediate-salinity transition. This result suggests that the salt concentration, and more generally long-range interparticle interactions, do not solely determine the flocculation process.

Sample	A	B	s_{CCC} (PSU)	D
E39(S3)	0.12 ± 0.01	0.53 ± 0.15	1.19 ± 0.35	0.88 ± 0.01
E16	0.22 ± 0.02	0.58 ± 0.13	0.36 ± 0.07	0.74 ± 0.02
RV555	0.27 ± 0.01	1.15 ± 0.08	1.60 ± 0.05	0.71 ± 0.01
RV555K	0.19 ± 0.02	0.60 ± 0.17	0.86 ± 0.18	0.81 ± 0.02
Fv49	~ 0	0.83 ± 1.45	0.41 ± 0.48	0.98 ± 0.01

Table 2: Parameters obtained by fitting the error function (Eq. 2) at $T = 4$ h for E39(S3), E16, RV 555, RV 555 K, and Fv 49 (chrysotile).

3.2. Microscopy-derived particle morphology

Microscopic observations provide direct evidence of the morphological diversity of the investigated sediments. Individual particles may display a wide range of shapes, from angular fragments to elongated grains, confirming that the primary particles deviate substantially from spherical reference geometry. This is especially true and important for the rock-blasted fine-grained sediment analyzed in this study. Direct imaging further enabled quantification of particle-size and aspect-ratio distributions, revealing marked site-to-site variability in both characteristic dimensions and degree of irregularity.

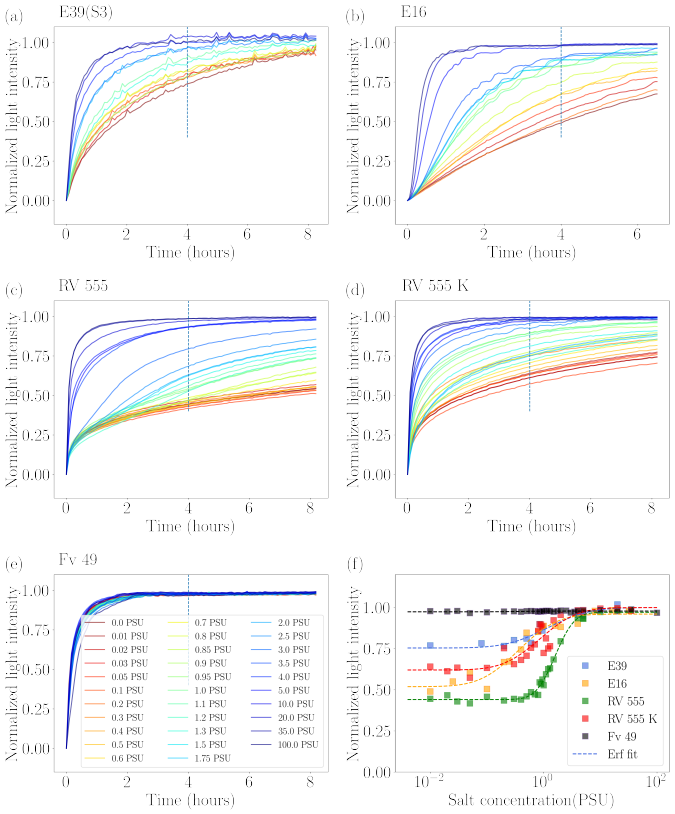

Figure 3: Time evolution of normalized transmitted light intensity for sediments collected at different sites and salinities. Panels (a)–(e) show the temporal evolution of I_{norm} for E39(S3), E16, RV 555, RV 555 K, and Fv 49, respectively. The vertical dashed line indicates the comparison time $T = 4$ h. Panel (f) shows I_{norm} at $T = 4$ h as a function of salinity; dashed lines represent fits to Eq. 2.

Representative microscopy images of the different sediment samples are shown in Fig. 4. The images highlight clear contrasts in particle size, angularity, and aspect ratio between sites. Qualitatively, the RV 555 K and E16 samples appear to be dominated by smaller and more compact grains, while Fv 49 and E39(S3) show a higher prevalence of larger and more elongated particles. These observations are consistent with the quantitative microscopy analysis given further below and may provide direct physical insight into why the bulk-settling response remains site-dependent, particularly at low salinity, where salt-induced destabilization is weaker.

The quantitative particle-size and aspect-ratio distributions derived from microscopy are summarized in Fig. 5. As a general trend, most samples are dominated by the fraction of fine particles in the range of 2.0–6.3 μm. At the same time, clear inter-site differences emerge in both the breadth of the size of the distributions and the prevalence of elongated grains. In particular, E39(S3) and Fv49 exhibit broader distributions together with more pronounced tails of high aspect ratios, indicating a greater contribution of elongated particles and a more morphologically diverse population. By contrast, RV 555 and E16 are characterized by narrower distributions dominated by smaller, more compact, and more equant grains. The remaining samples occupy intermediate regimes, with mixed populations of compact and elongated particles. Overall, these results indicate that the investigated sediments differ not only in characteristic particle size, but also in particle shape, which is expected to influence interparticle contacts, aggregation pathways, and ultimately settling behavior.

To quantify this morphological variability in a compact manner, we define a Morphology–Size Index ($\mathcal{M}$) from the joint distribution of particle size d and aspect ratio α. Let Ω_{90} denote the smallest region in the (d, α) plane containing 90% of the detected particles. We then define

$$d_{90}^{\max} = \max_{(d,\alpha)\in\Omega_{90}} d, \qquad \alpha_{90}^{\max} = \max_{(d,\alpha)\in\Omega_{90}} \alpha, \tag{3}$$

and

$$\mathcal{M} = d_{90}^{\max}\, \alpha_{90}^{\max} \quad . \tag{4}$$

Here, $d_{90}^{\max}$ represents the largest particle size within the dominant 90% population, while $\alpha_{90}^{\max}$ represents the largest aspect ratio within that same population. By construction, $\mathcal{M}$ emphasizes the upper extent of size and elongation in the main particle population while remaining less sensitive to rare outliers.

The scatter plots in Fig. 6(a)–(e) illustrate how this descriptors d and α capture the geometric contrast between samples. For example, RV 555 and E16 are characterized by a relatively compact distribution, concentrated at smaller particle sizes and lower aspect ratios, and therefore yields a comparatively small $\mathcal{M}$ represented in Fig. 6(f). By contrast, Fv 49 shows a broader distribution extending to larger particle sizes and higher aspect ratios, consistent with substantially larger $\mathcal{M}$. E39(S3) also exhibits an extended contour with a pronounced tail toward elongated particles, while RV 555 K occupy an intermediate regime, with more moderate extensions in size and aspect ratio. In this sense, $\mathcal{M}$ is condensed into a single parameter to describe whether the dominant particle population is mainly composed of small, compact grains or includes substantial fractions of larger and more elongated particles.

As shown in Fig. 6(f), $\mathcal{M}$ varies systematically between samples and correlates very well with the low-salinity bulk-settling plateau, $I_{\mathrm{norm}}^{s\to 0}$. This correlation is particularly relevant because the bulk-settling response is only weakly affected by changes in salinity for low salt concentrations, indicating that electrostatic screening, referring as the reduction in the range and magnitude of the electrostatic interaction in between particle cause by the presence of ions in the surrounding solvent, is not yet the dominant control. The correlation therefore indicates that the site-specific low-salinity clarification response is systematically associated with primary-particle geometry. In particular, samples with larger values of $\mathcal{M}$, i.e. samples containing a more extended population of larger and/or more elongated grains, tend to exhibit a distinct low-salinity settling response. This trend suggests that particle morphology may facilitate early-stage entanglement, interlocking, or loose aggregation of primary particles into more developed flocs, thereby enhancing the collective settling behavior even before strong salt-induced destabilization becomes important.

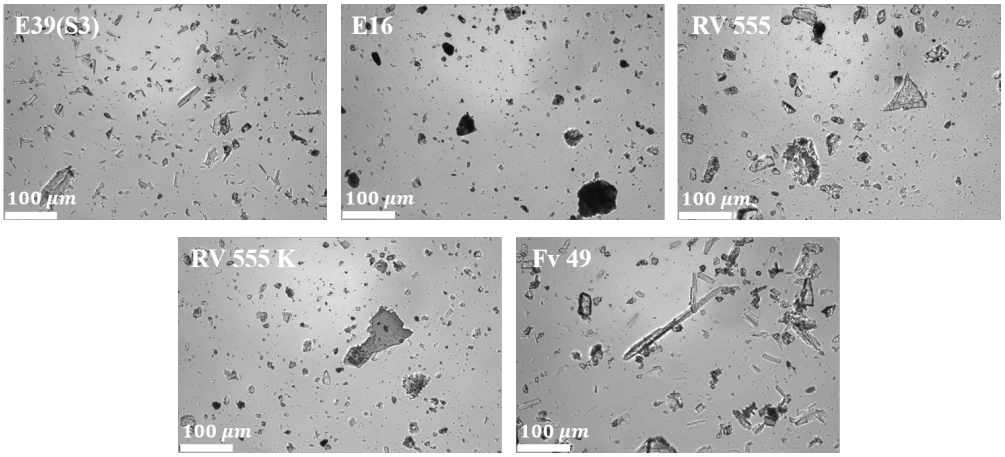

Figure 4: Microscopic images of natural sediment samples collected from different locations: E39, E16, RV555, RV 555 K, and Fv49. The micrographs reveal the morphological diversity of particles, ranging from fine angular fragments to larger aggregates and elongated grains. The scale bar in each panel corresponds to 100 μm

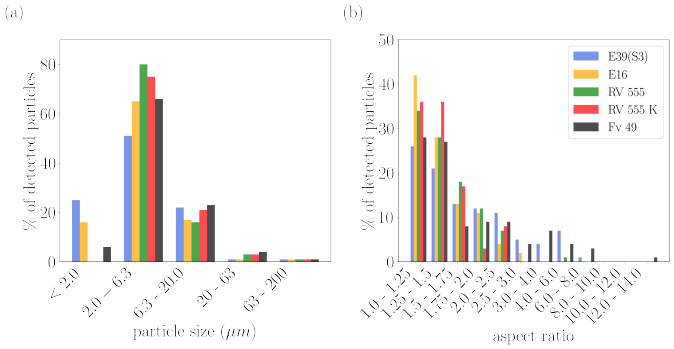

Figure 5: Microscopy-based distributions of primary-particle morphology for sediments collected at five tunnel sites. (a) Particle-size distributions obtained from direct microscopy. (b) Aspect-ratio distributions for the same samples. The results highlight clear site-to-site differences in both characteristic particle size and particle elongation, supporting the interpretation that morphology contributes to the site-dependent bulk-settling response.

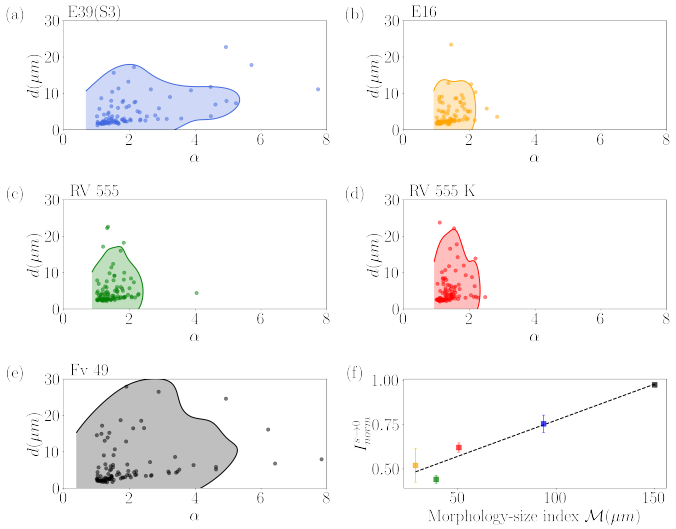

Figure 6: Microscopy-based morphology–size characterization of the investigated sediments. Panels (a)–(e) show scatter plots of particle size versus aspect ratio for each site (E39(S3), E16, RV 555, RV 555 K and Fv 49). The shaded contour encloses the core of the distribution (90% of the data points), highlighting the dominant morphology range of the primary particle population. Panel (f) summarizes the morphology–size index ($\mathcal{M}$), defined from the contour extrema as $\mathcal{M} = d_{90}^{\max} A_{90}^{\max}$, plotted against the low-salinity bulk-settling plateau $I_{\mathrm{norm}}^{s\to 0}$; the dashed line indicates a linear fit and error bars denote the uncertainty on $I_{\mathrm{norm}}^{s\to 0}$.

3.3. ζ-potential response to salinity

The morphology-based analysis above indicates that particle shape contributes to the low-salinity baseline of the bulk-settling response. As salinity increases, however, electrostatic screening becomes a progressively more important control parameter for the bulk settling behavior, particularly in the vicinity of the characteristic transition that occurs at salinity s_{CCC} identified in Fig. 3. In this regime, electrostatic interactions between particles are expected to play an increasingly important role in suspension stability and in the onset of salinity-driven coagulation and flocculation. Because mineral particles in water generally carry a net surface charge balanced by an electrical double layer of characteristic thickness κ^{-1}, known as the Debye length [22], changes in salt concentration can strongly modify the range of interparticle repulsion. At low salinity, the electrical double layer extends farther into the fluid, leading to stronger repulsive interactions and, therefore, limited aggregation. As salinity increases, dissolved ions compress the diffusive double layer and screen repulsive forces, thereby reducing the energy barrier for particle–particle contact and promoting coagulation and floc formation. In this sense, the measured electrokinetic response provides a bridge between the mineralogical nature of the particles and the salinity dependence of the bulk-settling behavior.

To quantify this electrostatic contribution, we measured the ζ-potential, which provides an operational proxy for the magnitude of the electrostatic repulsion between particles, by measuring the electrical potential in the hydrodynamic slipping plane. More negative ζ-potential values indicate stronger electrostatic stabilization, while values approaching zero reflect weaker re-

pulsion and therefore a higher propensity to aggregation.

Figure 7(a) shows the salinity dependence of the measured ζ-potential for the investigated sediments. All samples display a non-trivial response to salinity, but the magnitude and shape of that response differ between sites. In particular, the low-salinity baseline remains relatively similar across several samples, whereas the amplitude of the salinity-induced variation differs substantially. This indicates that the initial electrokinetic state is not strongly separated between all materials, while the way in which the suspensions respond to increasing salinity is clearly site dependent.

To capture these trends in a compact form, the data were fitted with an empirical expression consisting of a hyperbolic-tangent transition centered at s_0, being the salt concentration where the $\zeta-$potential presents a sharp drop from the low salinity plateau, combined with a gated linear contribution that becomes active only for $s > s_0$:

$$\zeta(s) = a + b\ \tanh[c\,(s - s_0)] + g\,(s - s_0)\,\Theta(s - s_0)\,, \qquad (5)$$

where

$$\Theta(s) = \frac{1}{2}\,[1 + \tanh(s)]\,, \qquad (6)$$

correspond to a smoothed Heaviside step function. In this formulation, the hyperbolic-tangent term captures the sharp drop in ζ-potential around the characteristic salinity s_0, while the gated linear term $g(s - s_0)\Theta(s - s_0)$, accounts for the approximately linear evolution observed after this transition. The function $\Theta(s)$ ensures that this linear contribution is effectively suppressed for $s < s_0$ and progressively activated for $s > s_0$, thereby providing a continuous representation of the sudden drop followed by a distinct post-transition regime. Here, a, b, c, s_0 and g denote the fitting parameters, whose values are summarized in Table 3. Salinity points were selected approximately logarithmically to resolve rapid variations at salt concentration while retaining coverage up to the higher values of salinity (35 PSU). The purpose of this fit is not to provide a mechanistic description of surface charge but rather to extract reproducible descriptors of the electrokinetic response that can be compared across samples.

Sample	a (mV)	b (mV)	c (PSU^{-1})	s_0 (PSU)	g (mV PSU^{-1})
E39(S3)	-39.8200	-5.9137	33.3068	0.8488	0.6419
E16	-39.5105	-9.6272	33.3419	0.7008	1.0014
RV 555	-42.0535	-11.2535	18.1875	0.7000	0.9143
RV 555 K	-28.2140	-19.1214	1.2929	–	0.9689
Fv 49	-14.6601	-9.8714	3.2728	–	0.6882

Table 3: Fitting parameters of the empirical ζ-potential model (Eq.5) for each sediment sample. "–" = values close to zero.

A pronounced change in ζ-potential occurs over the intermediate salinity range associated with the bulk-settling transition (Fig. 7(a)), particularly for RV 555 and E16. As salinity approaches the operational s_{CCC}, visible flocs form and settle on timescales of $O(10)$ s, substantially shorter than the approximately 120 s required for a ζ-potential acquisition. Consequently, the measured signal becomes increasingly dominated by the smaller particles that remain suspended after the rapidly settling aggregates have been removed. The pronounced decrease relative to the low-salinity plateau in the ζ-potential measurement showed in Fig. 7(a), $\zeta^{s\to0}$, should therefore be interpreted as an electrokinetic signature of this residual fine fraction rather than as evidence that the entire suspension becomes more stable. At low salinity, where aggregation and settling are weaker, the measurement samples a broader particle population. At intermediate salinity ($s \approx 1$), flocculation selectively removes the more readily aggregating particles, leaving a comparatively stable fine fraction in suspension. The magnitude of this apparent ζ-potential drop, $\Delta\zeta_{\mathrm{min}}$ correlates with the bulk-settling amplitude A (Fig. 7(b)), linking the electrokinetic response of the residual suspended fraction to the onset of enhanced macroscopic clarification. Despite this limitation, ζ-potential measurements clearly show that the investigated sediments exhibit distinct electrokinetic responses to salinity, consistent with differences in mineralogical composition and fine-fraction surface chemistry. To quantify the salinity-induced destabilization, we define

$$\Delta\zeta_{\mathrm{min}} = \min(\zeta - \zeta^{s\to0}), \qquad (7)$$

This quantity measures the maximum salinity-driven reduction in electrostatic potential relative to the low-salinity state and therefore provides a simple descriptor of how strongly each sediment responds to increasing salt concentration.

Figure 7(b) shows that the magnitude of this electrostatic drop correlates with the bulk-settling fit parameter A. In other words, samples exhibiting a stronger salinity-induced reduction in ζ-potential also tend to show a greater increase in bulk clarification between the low and high-salinity regimes. This result provides an important link between the electrokinetic measurements and the macroscopic settling response. At the same time, it should be noted that the low-salinity, ζ-potential baseline $\zeta^{s\to0}$ remains comparatively similar between samples, while the low-salinity bulk-settling plateau differs much more strongly between sites. This contrast supports the view that electrostatic effects become increasingly important as salinity increases, while morphology plays a more prominent role in setting the baseline settling behavior under low salinity. In parallel, the low-salinity settling plateau $I^{s\to0}_{\mathrm{norm}}$ varies between samples and correlates with the morphology–size index ($\mathcal{M}$), reinforcing the interpretation that particle geometry contributes primarily to baseline settling and weak aggregation when salt concentration is still not sufficient to promote strong salt-driven flocculation.

4. Discussion

The results show that the bulk-settling response of tunnel-derived fine-grained blasted sediments is strongly dependent on salinity, but that the origin of this dependence is not the same in all salinity regimes. In particular, the combined analysis indicates that morphology and electrostatic interactions contribute differently to the settling response and that their relative importance changes with salt concentration. At low salinity, where

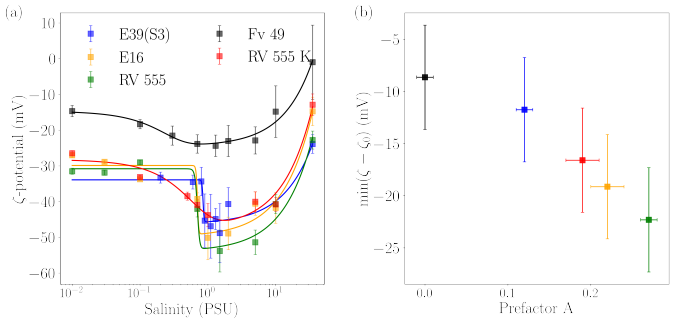

Figure 7: Salinity dependence of the ζ-potential for the investigated sediments. (a) measured $\zeta(s)$ for E39, E16, RV 555, Fv 49, and RV 555K; solid lines show fits using the empirical smooth-step model (Eq. 5). (b) comparison of the bulk-settling transition parameter A with the electrokinetic response magnitude $\Delta\zeta_{\min} = \min(\zeta - \zeta^{s\to 0})$, where $\zeta^{s\to 0}$ is the low-salinity baseline; error bars indicate uncertainties in A and in $\Delta\zeta_{\min}$.

electrostatic screening remains weak, inter-site differences in settling are clearly observed, showing that the baseline clarification response cannot be explained by salinity alone. As salinity increases toward the transition regime, electrostatic destabilization becomes more important and progressively promotes flocculation, hence increasing the settling speed.

Figure 7(a) shows that the low-salinity baseline of the ζ-potential remains relatively similar between samples, despite their contrasting mineralogical compositions. Within the resolution of the present measurements, this suggests that mineralogy does not strongly differentiate the initial electrokinetic state under weakly saline conditions. In contrast, the bulk-settling response at low salinity, shown in Fig. 3(f), exhibits pronounced site-dependent differences. Together, these observations are consistent with the interpretation that low-salinity settling is influenced more strongly by particle morphology than by differences in the initial electrostatic state. Thus, variations in particle size and shape have the potential to affect both the settling dynamics of individual grains and the early-stage aggregation pathways that set the baseline clarification response before strong salt-induced destabilization becomes dominant. This interpretation is consistent with the observations of [2], who showed that the onset of rapid clay settling is promoted by salinity, while the subsequent settling dynamics remain strongly dependent on suspended-particle concentration. Their results therefore reinforce that the bulk clarification response cannot be attributed to salt concentration conditions alone.

These morphological differences are physically relevant because primary-particle geometry can influence the orientation and persistence of particle contacts during the early stages of aggregation. Numerical results for complex-shaped colloids have shown that geometric interlocking and entanglement can promote persistent particle associations even without attractive surface interactions [20]. In the present experiments, this provides a plausible mechanism through which primary-particle morphology may contribute to the site-dependent low-salinity clarification response before strong salt-induced destabilization develops. Once aggregates form, their resulting three-dimensional morphology introduces an additional hydrodynamic control. [19] showed that natural flocs are substantially more irregular and complex than inferred from conventional two-dimensional descriptors and that 2D-based approximations can strongly overestimate floc size and mass settling flux, particularly for macroflocs ($D > 160\ \mu$m). Studies on natural sediments further indicate that settling behavior is site dependent and cannot be described by size alone, since structural properties such as porosity and shape also contribute to floc settling dynamics [18]. Consistently, recent studies have identified aggregate permeability as an additional key parameter controlling hydrodynamic resistance and settling velocity, further emphasizing that floc size alone is insufficient to describe the settling dynamics of porous aggregates [21, 23].

Taken together, these observations suggest that morphology can influence settling across scales, from primary-particle contact formation to the hydrodynamics of the resulting flocs. In our experiments, this influence is reflected directly in the correlation between the morphology–size index $\mathcal{M}$ and the low-salinity clarification plateau. At low salinity, where the settling response is only weakly affected by changes in interparticle repulsion, the bulk-settling curves exhibit a quasi-salinity-independent plateau whose level differs systematically between samples (Fig. 3f).

In this sense, $\mathcal{M}$ provides a compact empirical descriptor of how the dominant particle population combines size and elongation in a way that appears to influence early-stage floc development in the low-salinity regime.

Further insight is obtained from the empirical fit introduced for the normalized transmitted light intensity in Eq. 2. In the low-salinity limit, $s \to 0$, the argument of the error function tends to large negative values and therefore erf $\to -1$, giving

$$I_{\text{norm}}^{s\to 0} = D - A. \tag{8}$$

In the high-salinity limit, $s \to \infty$, one has erf $\to 1$, yielding

$$I_{\text{norm}}^{s\to \infty} = D + A = 1, \tag{9}$$

since the data are normalized such that the high-salinity plateau tends to unity. Combining Eqs. 8 and 9 shows that the prefactor A controls half of the transition amplitude between the low- and high-salinity plateaus:

$$A = \frac{1}{2}\left(I_{\text{norm}}^{s\to\infty} - I_{\text{norm}}^{s\to 0}\right) = \frac{1}{2}\left(1 - I_{\text{norm}}^{s\to 0}\right). \tag{10}$$

The linear regression between $\mathcal{M}$ and the low-salinity plateau $I_{\text{norm}}^{s\to 0}$, presented in Fig. 6(f), yields

$$I_{\text{norm}}^{s\to 0} = \lambda\,\mathcal{M} + \beta_0, \tag{11}$$

with $\lambda \approx 4 \times 10^{-3}\ \mu\text{m}^{-1}$ and $\beta_0 \approx 0.37$. Using Eq. 10, this relation can be rewritten as

$$A = \frac{1}{2}\left[1 - (\lambda\,\mathcal{M} + \beta_0)\right]. \tag{12}$$

Together, these relations support a morphology-based interpretation of the low-salinity regime, in which $\mathcal{M}$ provides a first-order descriptor of the baseline settling response.

Eq. 12 can be interpreted as evidence that morphology preconditions the settling response in the low-salinity regime. In this framework, not only does morphology affect the settling speed in this regime, but also it constrains how much room remains for subsequent salt-induced enhancement. This conclusion is strongly supported by the dataset collected at various sites with different geological conditions, which shows that sediments with different morphological and mineralogical signatures also exhibit different baseline clarification responses at low salinity. The coefficient λ therefore quantifies the empirical sensitivity of the low-salinity plateau to changes in $\mathcal{M}$, while Eq. 12 implies a corresponding reduction of the transition amplitude, with $(dA/d\mathcal{M}) = -\lambda/2$. In this sense, λ can be viewed as a measure of morphological leverage: the increase in the contribution of morphology enhances clarification, but correspondingly reduces the remaining gain available from salinity-driven destabilization. Within this interpretation, β_0 is best regarded as an extrapolated fitting parameter rather than a material constant with direct physical meaning.

At higher salinity, the bulk-settling response becomes increasingly sensitive to salt concentration and to the interaction between mineral surfaces and the surrounding electrolyte. Although settling remains influenced by primary-particle morphology and by the geometry of the resulting flocs, electrostatic screening progressively reduces interparticle repulsion and promotes enhanced aggregation and clarification. This salinity-dependent response is evident in Fig. 3 and is consistent with previous observations of enhanced flocculation and settling with increasing salt concentration in cohesive sediment and clay suspensions [2, 15, 16, 24]. Similar changes in floc size and structure have also been reported for natural cohesive sediments, with the magnitude of the response additionally depending on the imposed turbulent shear [25].

Because the dominant changes in settling occur over several orders of magnitude in salinity, the transition is more naturally analyzed as a function of $\log_{10}(s)$ than of s itself. The relevant control parameter is therefore not a fixed additive increase but a multiplicative change in salt concentration. The sensitivity of the settling response to such changes in salinity can consequently be quantified by differentiating Eq. 2 with respect to $\log_{10}(s)$:

$$\frac{dI_{\mathrm{norm}}}{d\log_{10}(s)} = \frac{2AB}{\sqrt{\pi}} \exp\left[-\left(B\log_{10}\left(\frac{s}{s_{\mathrm{CCC}}}\right)\right)^2\right]. \tag{13}$$

This expression shows that the response is localized around the characteristic transition salinity s_{CCC}, and that its magnitude depends jointly on the transition amplitude A and the empirical steepness parameter B.

The slope reaches its maximum at the inflection point $s = s_{\mathrm{CCC}}$, where $\log_{10}(s/s_{\mathrm{CCC}}) = 0$, giving

$$\left.\frac{dI_{\mathrm{norm}}}{d\log_{10}(s)}\right|_{s=s_{\mathrm{CCC}}} = \frac{2AB}{\sqrt{\pi}}. \tag{14}$$

Thus, $2AB/\sqrt{\pi}$ provides a compact measure of how rapidly the settling response changes per multiplicative change in salinity, while $2A$ represents the total amplitude of the transition between the low- and high-salinity plateausand is empirically related to the morphological parameter $\mathcal{M}$ as it was discussed previously. Accordingly, B alone should not be interpreted as the overall sensitivity of clarification to salt concentration, but rather as a geometrical measure of the sharpness of the normalized transition in logarithmic salinity space. In contrast, the product AB determines the absolute sensitivity of the clarification response, since it combines the transition sharpness with its total amplitude. Thus, B describes how abruptly the normalized transition occurs, whereas AB quantifies how strongly clarification changes with salinity around s_{CCC}.

Recalling the values of the parameters determined for the error function (Eq. 2) fitted for data from the various sites as summarized in Table 2, the comparison between E16 and RV 555 illustrates the different information conveyed by the fit parameters. Although their transition amplitudes A are of comparable magnitude, E16 exhibits a smaller B and a substantially lower s_{CCC}. Its salinity-dependent response therefore begins at lower salt concentration and develops more gradually over a broader salinity range. In contrast, RV 555 displays a transition centered at higher salinity and characterized by a larger B, corresponding to a later but sharper transition to salinity. The larger salinity-induced decrease in ζ-potential observed for RV 555 is consistent with its greater transition amplitude, but does not by itself account for the higher value of s_{CCC}. Because s_{CCC} is derived from the bulk-settling response at the fixed observation time $T = 4$ h, it should be interpreted as an operational kinetic descriptor that integrates the combined effects of electrostatic screening, particle morphology, aggregation kinetics, and the settling timescale of the resulting flocs. The interpretation of these differences must explicitly account for the selected observation time. The salinity-dependent curves in Fig. 3(f) represent an isochronal comparison at $T = 4$ h, rather than an equilibrium stability diagram. This time was selected because the highest-salinity suspensions had essentially completed their clarification, whereas the low- and intermediate-salinity conditions remained sufficiently separated to allow meaningful intersite comparison. Consequently, the fitted quantities $A(T)$, $B(T)$, and $s_{\mathrm{CCC}}(T)$ should be regarded as time-dependent operational descriptors rather than intrinsic material constants. At longer times, continued clarification of the weakly saline suspensions would reduce the contrast between the low- and high-salinity plateaus and hence decrease $A(T)$, while $B(T)$ and $s_{\mathrm{CCC}}(T)$ may also evolve as the relative settling kinetics change. Nevertheless, testing different values of T allows us to conclude that the sensitivity of T remains low and the reported values are good first order approximations for the critical coagulation concentration s_{ccc} [c.f. 15]. Importantly, the combined analysis of bulk settling behavior as well as particle size, shape, and ζ-potential reveals a consistent physical picture for the sediment types investigated in this study. Primary-particle morphology establishes the low-salinity clarification state and thereby conditions the macroscopic range over which salinity can further enhance settling. As salt concentration increases, electrostatic screening reduces interparticle repulsion, promotes floc formation, and progressively activates this remaining clarification potential. The observed correlations therefore support a coupled

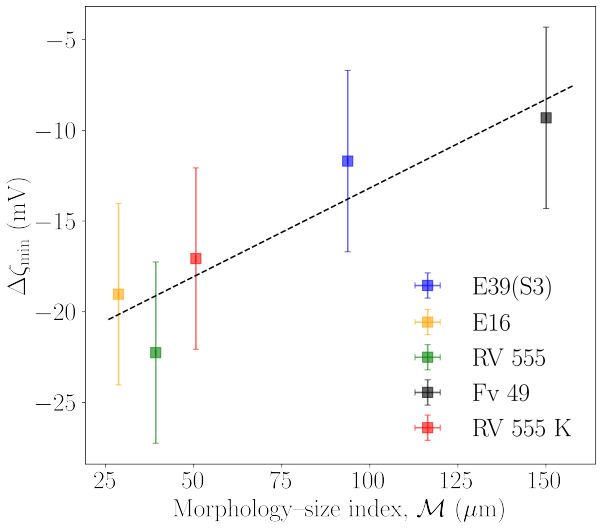

Figure 8: Relationship between the morphology–size index $\mathcal{M}$ and the salinity-induced change in ζ-potential, $\Delta\zeta_{\min}$, for the investigated sediment samples. Symbols denote the different tunnel sites and error bars represent the uncertainty associated with $\mathcal{M}$ and $\Delta\zeta_{\min}$. The dashed line indicates the linear regression as a guide to the eye.

interpretation in which morphology conditions the low-salt concentration settling configuration, while the electrokinetic response is associated with the magnitude and characteristic development of the salinity-induced enhancement. Despite the time dependence of the fitted parameters, the principal outcome remains robust: salinity improves bulk clarification by strengthening flocculation, but the extent and pathway of this improvement are conditioned by the morphology of the initial particle population.

The relation shown in Fig. 8 further suggests that the electrokinetic response observed in the transition regime is not independent of the initial particle morphology. Samples characterized by larger values of $\mathcal{M}$ tend to exhibit a smaller-magnitude $\Delta\zeta_{\min}$, whereas sediments dominated by smaller and more compact primary particles generally display a stronger apparent electrokinetic change. This trend is consistent with a population-selection mechanism. At low salinity, particle morphology conditions the initial settling and weak aggregation response, thereby determining the particle population that remains available for salt-induced flocculation. As salinity approaches s_{CCC}, the particles that aggregate most efficiently form larger flocs and are rapidly removed from suspension, progressively leaving a finer and potentially more electrostatically stable residual population. The measured $\Delta\zeta_{\min}$ therefore reflects not only the response to increasing salt concentration, but also the morphology-conditioned evolution of the suspended particle population.

5. Conclusions

This study demonstrates that bulk clarification of tunnel-derived, rock-blasted fine-grained sediments is controlled by the coupled effects of primary particle morphology and salinity-dependent electrokinetic screening. The relative importance of these mechanisms changes throughout the investigated salinity range. In the low-salinity regime, the settling response remains closely independent of salt concentration but differs substantially among sampling sites. The correlation between the morphology–size index $\mathcal{M}$ and the low-salinity clarification plateau in Fig. 6(f), formalized through Eq. 12, identifies primary-particle size and elongation as first-order descriptors of early clarification, specifically, for suspensions with low salt concentration. Sediments containing larger and more elongated particle populations tend to reach a higher clarification state before strong salt-induced destabilization develops. This observation is consistent with morphology influencing individual-particle settling, interparticle contacts, and early aggregate formation.

The comparison between E16 and RV 555 further distinguishes the morphology-controlled baseline from the subsequent salinity-dependent response. These sediments exhibit comparatively similar morphology–size indices and relatively low-salinity clarification levels, but their settling responses differ markedly at intermediate salinities ($0.1 \lesssim s \lesssim 5$ (PSU)). E16 responds at lower salinity and undergoes a broader transition, whereas RV 555 remains less clarified until higher salinity is reached (≈ 1 (PSU)) and subsequently develops a sharper response. This comparison shows that primary-particle morphology provides an important constraint on the initial clarification state, does not alone determine the salinity range or sharpness of the clarification transition over which enhanced flocculation develops. The coupling between these mechanisms is further supported by Fig. 8, which shows that the magnitude of the salinity-induced electrokinetic response varies systematically with the initial morphology–size index. This trend is consistent with a selective aggregation mechanism in which primary-particle morphology conditions the population available for flocculation, while increasing salt concentration screens electrostatic repulsion and preferentially removes the particles that aggregate most readily. The resulting clarification transition therefore reflects the combined action of particle geometry and electrostatic screening, rather than two independent controls.

At salinities above approximately 10 PSU, the settling responses converge toward a common high-clarification state, indicating that further increases in salt concentration provide little additional enhancement under the present experimental conditions.

Mineralogical characterization confirms that the investigated sediments originate from contrasting mineral assemblages. However, these compositional differences are not accompanied by equally pronounced differences in the low-salinity ζ-potential baseline, indicating that bulk mineralogy alone does not explain the initial electrokinetic state or the site-dependent clarification observed in this regime. Mineralogical composition and fine-fraction surface chemistry may nevertheless contribute to the distinct electrokinetic responses observed at intermediate salinities, where particle–electrolyte interactions become increasingly important.

Overall, the results support a coupled and salinity-dependent picture of fine-sediment clarification. Primary-particle morphology conditions the low-salinity settling state and the par-

ticle population available for subsequent aggregation, whereas increasing salt concentration screens electrostatic repulsion and promotes selective flocculation of this population. The fitted quantities $A(T)$, $B(T)$, and $s_{CCC}(T)$ remain operational descriptors evaluated at $T = 4$ h rather than intrinsic material constants; however, this does not alter the central observation that morphology and electrostatic screening act jointly to determine the magnitude and pathway of clarification. Future work should determine how this coupling evolves under changes in pH and imposed shear, and directly relate floc size and structure to settling velocity. For tunnel-derived fine sediments discharged into receiving waters, salinity alone is therefore insufficient to predict settling, and the properties of the initial particle population must also be considered.

Acknowledgements

The authors gratefully acknowledge Tahoora Mesgari, Juan Carlos Schöder, Arsha Valsala Soman, and Renjana Varikkattu Soman for their contributions to the SAILOR project through experimental work, sample characterization, and ζ-potential measurements. Their work during student and thesis projects contributed to the experimental and methodological basis on which the present study was developed. The authors also gratefully acknowledge the Norwegian Public Roads Administration (Statens vegvesen) for funding the SAILOR project and for providing the sediment samples and relevant information from the investigated tunnel construction sites.

References

[1] J. Winterwerp, W. van Kesteren, Introduction to the Physics of Cohesive Sediment Dynamics in the Marine Environment, Vol. 56 of Developments in Sedimentology, Elsevier, Amsterdam, 2004.

[2] B. Sutherland, K. Barrett, M. Gingras, Clay settling in fresh and salt water, Environ. Fluid Mech. 15 (2015) 147–160. doi:10.1007/s10652-014-9365-0.

[3] X. Kang, Z. Xia, R. Chen, P. Liu, W. Yang, Effects of inorganic cations and organic polymers on the physicochemical properties and microfabrics of kaolinite suspensions, Appl. Clay Sci. 176 (2019) 38–48. doi:10.1016/j.clay.2019.04.024.

[4] P. Bertsch, J. Seaman, Characterization of complex mineral assemblages: Implications for contaminant transport and environmental remediation, Proc. Natl. Acad. Sci. U.S.A. 96 (1999) 3350–3357. doi:10.1073/pnas.96.7.3350.

[5] J. Ren, A. Packman, Modeling of simultaneous exchange of colloids and sorbing contaminants between streams and streambeds, Environ. Sci. Technol. 38 (10) (2004) 2901–2911. doi:10.1021/es034852l.

[6] L. Mevenkamp, T. Stratmann, K. Guilini, L. Moodley, D. van Oevelen, A. Vanreusel, S. Westerlund, A. Sweetman, Impaired short-term functioning of a benthic community from a deep norwegian fjord following deposition of mine tailings and sediments, Front. Mar. Sci. 4 (2017) 169. doi:10.3389/fmars.2017.00169.

[7] K. Mathers, A. Doretto, S. Fenoglio, M. Hill, P. Wood, Temporal effects of fine sediment deposition on benthic macroinvertebrate community structure, function and biodiversity likely reflects landscape setting, Sci. Total Environ. 829 (2022) 154612. doi:10.1016/j.scitotenv.2022.154612.

[8] M. Mooselu, H. Liltved, N. Akhtar, Characterization and treatment of tunneling wastewater using natural and chemical coagulants, Water Sci. Technol. 88 (10) (2023) 2547–2565. doi:10.2166/wst.2023.363.

[9] O. Neshamar, A. Cuthbertson, Ø. Thiem, P. Davies, Laboratory investigation of polydisperse rock releases into deep receiving waters through vertical, enclosed fall-pipes, Applied Ocean Research 168 (2026) 104957. doi:10.1016/j.apor.2026.104957.

[10] D. Swift, S. Friedlander, The coagulation of hydrosols by brownian motion and laminar shear flow, J. Colloid Sci. 19 (7) (1964) 621–647. doi:10.1016/0095-8522(64)90085-6.

[11] P. Saffman, J. Turner, On the collision of drops in turbulent clouds, J. Fluid Mech. 1 (1) (1956) 16–30. doi:10.1017/S0022112056000020.

[12] I. Valioulis, E. List, Collision efficiencies of diffusing spherical particles: Hydrodynamic, van der Waals and electrostatic forces, Adv. Colloid Interface Sci. 20 (1) (1984) 1–20. doi:10.1016/0001-8686(84)80001-9.

[13] B. Logan, Environmental Transport Processes, 2nd Edition, John Wiley & Sons, Hoboken, NJ, 2012. doi:10.1002/9781118230107.

[14] J. Gregory, Particles in Water: Properties and Processes, CRC Press, Boca Raton, FL, 2006. doi:10.1201/9780203508459.

[15] E. Krahl, B. Vowinckel, L. Ye, T.-J. Hsu, A. Manning, Impact of the salt concentration and biophysical cohesion on the settling behavior of bentonites, Front. Earth Sci. 10 (2022) 886006. doi:10.3389/feart.2022.886006.

[16] F. Mietta, C. Chassagne, A. J. Manning, J. C. Winterwerp, Influence of shear rate, organic matter content, ph and salinity on mud flocculation, Ocean Dyn. 59 (2009) 751–763. doi:10.1007/s10236-009-0231-4.

[17] A. Seiphoori, A. Gunn, S. Kosgodagan Acharige, P. E. Arratia, D. J. Jerolmack, Tuning sedimentation through surface charge and particle shape, Geophysical Research Letters 48 (2021) e2020GL091251. doi:10.1029/2020GL091251.

[18] N. D. Williams, D. E. Walling, G. J. L. Leeks, An analysis of the factors contributing to the settling potential of fine fluvial sediment, Hydrological Processes 22 (20) (2008) 4153–4162. doi:https://doi.org/10.1002/hyp.7015.

[19] K. Spencer, J. Wheatland, S. Carr, A. Manning, A. Bushby, C. Gu, L. Botto, T. Lawrence, Quantification of 3-dimensional structure and properties of flocculated natural suspended sediment, Water Res. 222 (2022) 118835. doi:10.1016/j.watres.2022.118835.

[20] F. B. Usabiaga, M. Ellero, Rheology of moderated dilute suspensions of star colloids: The shape factor, Phys. Fluids 36 (2024) 053321. doi:10.1063/5.0187721.

[21] A. Metelkin, B. Vowinckel, On the parameters of common settling velocity models for porous sediment aggregates, International Journal of Sediment Research 40 (3) (2025) 412–425.

[22] J. C. Berg, An introduction to interfaces and colloids: the bridge to nanoscience, World Scientific, 2010.

[23] A. Metelkin, B. Vowinckel, Effects of permeability on hindered settling of porous particles, arXiv preprint arXiv:2606.15182 (2026).

[24] N. Rommelfanger, B. Vowinckel, Z. Wang, R. Dohrmann, E. Meiburg, P. Luzzatto-Fegiz, A simple criterion and experiments for onset of flocculation in kaolin clay suspensions, arXiv preprint arXiv:2203.15545 (2022).

[25] R. G. Kumar, K. B. Strom, A. Keyvani, Floc properties and settling velocity of san jacinto estuary mud under variable shear and salinity conditions, Continental Shelf Research 30 (2010) 2067–2081. doi:10.1016/j.csr.2010.10.006.